

# Creep deformation behavior during densification of ZrB<sub>2</sub>-SiBCN ceramics with ZrO<sub>2</sub> additive

Bo FENG, Zhenhang WANG, Yunhao FAN, Jinghua GU, Yue ZHANG\*

*Key Laboratory of Aerospace Materials and Performance (Ministry of Education), School of Materials Science and Engineering, Beihang University, Beijing 100191, China*

Received: March 8, 2020; Revised: May 14, 2020; Accepted: May 29, 2020

© The Author(s) 2020.

**Abstract:** ZrB<sub>2</sub>-SiBCN ceramics with ZrO<sub>2</sub> additive are hot-pressed under a constant applied pressure. The densification behavior of the composites is studied in a view of creep deformation by means of the Bernard-Granger and Guizard model. With determination of the stress exponent ( $n$ ) and the apparent activation energy ( $Q_d$ ), the specific deformation mechanisms controlling densification are supposed. Within lower temperature ranges of 1300–1400 °C, the operative mechanism is considered to be grain boundary sliding accommodated by atom diffusion of the polymer-derived SiBCN ( $n = 1$ ,  $Q_d = 123 \pm 5$  kJ/mol) and by viscous flow of the amorphous SiBCN ( $n = 2$ ,  $Q_d = 249 \pm 5$  kJ/mol). At higher temperatures, the controlling mechanism transforms to lattice or intra-granular diffusion creep ( $n = 3-5$ ) due to gradual consumption of the amorphous phase. It is suggested that diffusion of oxygen ions inside ZrO<sub>2</sub> into the amorphous SiBCN decreases the viscosity, modifies the fluidity, and contributes to the grain boundary mobility.

**Keywords:** zirconium boride; polymer-derived SiBCN; creep deformation; densification mechanism; viscosity

## 1 Introduction

Zirconium boride (ZrB<sub>2</sub>) is characterized by extremely high melting point, high strength and hardness, chemical inertness against molten metals or slags, high electrical and thermal conductivities, and good oxidation resistance [1–3]. These outstanding properties make it an appropriate candidate for diverse applications, such as molten metal crucibles, electronic substrates, and thermal protective materials in the future hypersonic aviation system [4–6]. However, fully-dense ZrB<sub>2</sub> ceramic is difficult to fabricate due to its strong

covalent bonding and low self-diffusion coefficient [3]. The densification of this material has attracted extensive attention over these years.

Silicon or carbon containing materials such as SiC, Si<sub>3</sub>N<sub>4</sub>, C, B<sub>4</sub>C, and SiBCN, are generally introduced into ZrB<sub>2</sub> ceramic to significantly improve its sinterability, mechanical property, oxidation and ablation resistance [1,2,7–10]. SiC is recognized to be the preferred addition since it can effectively restrain the coarsening of ZrB<sub>2</sub> grains and enhance the comprehensive performance of the material [1,2]. Si<sub>3</sub>N<sub>4</sub> is able to react with B<sub>2</sub>O<sub>3</sub> originated from the surface of ZrB<sub>2</sub> powder, decrease vapor phase transport of boron oxide during sintering process, and help promote densification [7]. The introduction of carbon or carbides can also remove the surface oxide (ZrO<sub>2</sub> and B<sub>2</sub>O<sub>3</sub>) by carbothermal

\* Corresponding author.

E-mail: zhangy@buaa.edu.cn

reduction reactions and boost the solid-state sintering [8].

In our previous study, polymer-derived SiBCN was added into ZrB<sub>2</sub> powder and highly improved the sintering efficiency of ZrB<sub>2</sub> ceramic at medium temperature (below 1600 °C) under hot pressing conditions [10]. The multielement SiBCN ceramic underwent single-phase amorphous network, phase separation, and crystallization processes upon heat treatment. The crystallization products like SiC, Si<sub>3</sub>N<sub>4</sub>, C, and BN(C) were also effective sintering aids for the consolidation of ZrB<sub>2</sub> ceramics. The densification of ZrB<sub>2</sub>-SiBCN composites was mainly analyzed from a perspective of the significant influence caused by structural evolution of the additive (i.e., polymer-derived SiBCN) as well as chemical reactions occurred in the system. Actually, silicon-based polymer-derived ceramics (PDCs) possess viscoelastic property and sometimes they are called black glasses [11,12]. Riedel *et al.* [13,14] obtained a quite high creep viscosity of amorphous Si(B)CN under uniaxial compression and reported that a glass transition temperature was up to 1400–1500 °C and 1700 °C for SiCN and SiBCN, respectively. Creep was limited up to 1550 °C for Si(B)CN PDCs [11]. Although polymer-derived SiBCN cannot fully experience viscous flow resembling that of fused silica in a relatively low temperature range, its deformation and movement under pressure may be easier than those of crystal ceramic powder [15–17]. Therefore, SiBCN as a sintering aid may also contribute to promoting matter transportation of ZrB<sub>2</sub> by creep deformation, which is necessary to be researched in detail.

It is noted that ZrC formed in the final ZrB<sub>2</sub>-SiBCN samples by the reaction of ZrO<sub>2</sub> with carbon generated from polymer-derived SiBCN though some residual crystal ZrO<sub>2</sub> survived [10]. The specific interaction between oxides and PDCs at certain temperature has not been widely studied. Zhang *et al.* [18] reported that the addition of ZrO<sub>2</sub> into the mechanically-alloyed 2Si-B-3C-N powder was able to accelerate atom diffusion and promote the sintering process of the system. It was also demonstrated that ZrO<sub>2</sub> had remarkable influence on the crystallization and decomposition of polymer-derived SiOC ceramics [19]. It is deduced that oxides may enter the structure of PDCs and participate in their structural evolution since the obtained amorphous multielement phase after polymer pyrolysis has an open structure and wide chemical compatibility [10,11]. If the material system is exposed

under pressure, oxides may further affect the deformation behavior of PDCs. The role of ZrO<sub>2</sub> played in the densification progress of ZrB<sub>2</sub>-SiBCN composites is considered to be of interest.

Pressure-assisted sintering techniques like hot pressing (HP) and spark plasma sintering (SPS) are characterized by the simultaneous application of pressure and temperature [20,21]. The matter transportation during sintering is analogous to that occurring in high temperature creep [22,23]. The densification mechanism actually involves a creep deformation [24], which originates from a uniaxial macroscopic compaction pressure. Bernard-Granger and Guizard [22] proposed an analytical model in a view of the creep deformation to understand the sintering behavior of materials. This model was based on the steady state creep model which was established by Mukherjee *et al.* [25] in order to describe the creep of dense material. Thus it assumed that the major driving force during HP or SPS process was the macroscopic applied pressure. Given the porous-to-dense character during densification, the creep model was extended to sintering with some modifications. The modified expression for the dependence of the normalized densification kinetics on temperature, applied stress, and microstructural evolution is given by Eq. (1):

$$\frac{1}{\mu_{\text{eff}}} \frac{1}{D} \frac{dD}{dt} = K_0 \frac{e^{-\frac{Q_d}{RT}}}{T} \left(\frac{b}{G}\right)^p \left(\frac{\sigma_{\text{eff}}}{\mu_{\text{eff}}}\right)^n \quad (1)$$

where  $D$  is the instantaneous relative density,  $t$  is the time,  $\sigma_{\text{eff}}$  is the instantaneous effective stress acting on the powder bed,  $\mu_{\text{eff}}$  is the instantaneous shear modulus of the powder bed,  $K_0$  is a constant,  $R$  is the gas constant,  $T$  is the sintering temperature,  $Q_d$  is the apparent activation energy of the mechanism controlling the densification,  $G$  is the grain size,  $b$  is the Burgers vector,  $p$  is the exponent for grain size, and  $n$  is the exponent for stress. For a porous body, the assessment of  $\sigma_{\text{eff}}$  and  $\mu_{\text{eff}}$  is based on the instantaneous variation in porosity. They can be described as following Eqs. (2) and (3) [26,27]:

$$\sigma_{\text{eff}} = \frac{1 - D_0}{D^2 (D - D_0)} \sigma_{\text{mac}} \quad (2)$$

$$\mu_{\text{eff}} = \frac{E_{\text{th}}}{2(1 + \nu_{\text{eff}})} \frac{D - D_0}{1 - D_0} \quad (3)$$

where  $D_0$  is the density of green body,  $\sigma_{\text{mac}}$  is the uniaxial macroscopic compaction pressure to the

powder bed.  $E_{th}$  is the Young's modulus of the theoretically dense material, and  $\nu_{eff}$  is the effective Poisson's ratio. When the grain size is constant, which generally occurs in certain temperature, holding time, or relative density ranges [20,22], Eq. (1) transforms into Eq. (4):

$$\frac{1}{\mu_{eff}} \frac{1}{D} \frac{dD}{dt} = K_1 \frac{e^{-\frac{Q_d}{RT}}}{T} \left( \frac{\sigma_{eff}}{\mu_{eff}} \right)^n \quad (4)$$

where  $K_1$  is a constant.

This approach has been employed in metallic alloy or typical oxide ceramic (e.g., zirconia and alumina etc.) systems [22,28–30] to identify the densification mechanisms by evaluating the creep parameters (i.e., stress exponent and apparent activation energy). Recently, Kashyap and Mitra [24] also applied this model to help analyze the densification kinetics of  $ZrB_2$ –SiC based composites sintered by SPS. Here it is expected that the applicability of Bernard-Granger and Guizard model can be extended to the pressure-assisted sintering of composited ceramic materials including relatively high creep phase.

In this work, a small amount of sol–gel derived  $ZrO_2$  is introduced into  $ZrB_2$ –SiBCN system and multi-phase composited  $ZrB_2$ –SiBCN– $ZrO_2$  ceramic is fabricated by hot pressing technique. The Bernard-Granger and Guizard model is employed here to evaluate the densification behaviors of the targeted composites which involve a sintering aid (polymer-derived SiBCN) with viscous glassy feature as well as an active second phase ( $ZrO_2$ ) derived from the gel precursor. The densification mechanisms at different temperatures or duration stages are revealed in a view of creep with the aid of determining the stress exponent and apparent activation energy. Different from conventional crystal powder additives, viscous flow of the amorphous SiBCN is enhanced by the diffusion of oxygen ions inside  $ZrO_2$ , which plays a key role in improving the deformation performance of  $ZrB_2$  based materials. The correlation between  $ZrO_2$  content and the densification of the system is also explored.

## 2 Experimental procedure

### 2.1 Synthesis of $ZrO_2$ gel

Zirconium oxychloride ( $ZrOCl_2 \cdot 8H_2O$ , 99% in purity, Jinke Fine Chemical Research Institute, Tianjin, China)

was used as the zirconium precursor. It was dissolved in deionized water under magnetic stirring and a solution formed with the concentration of 0.4 mol/L. The solution was heated by a water bath with the constant temperature of 60 °C. Then ammonium hydroxide (5 wt% in solution concentration) was introduced into the solution by drop wise addition and the white  $ZrO(OH)_2$  precipitate appeared. According to the reaction between ammonium hydroxide and zirconium oxychloride, the theoretical mole ratio of them is 2:1, but it was increased to 3:1 since excess ammonia is beneficial to the complete reaction. After 1 hour, the generated precipitate was washed repeatedly with deionized water to remove chloride ions. Subsequently, nitric acid (10 wt% in solution concentration) was added into the filtered precipitation. It was used as peptizing agent which was capable to disperse the precipitation by adjusting pH value. The mole ratio of nitric acid and zirconium oxychloride was 1:1.2, with slightly excessive nitric acid. Then a transparent and stable colloidal suspension formed. The system was aged at 80 °C for 12 h under reflux. The obtained sol was dried at 80 °C overnight in ambient air. Finally, the dried powder was calcined in a muffle furnace at 300 °C for 1 h to remove the residual water and acid. According to the XRD result (not shown here), the powder after calcination was mainly amorphous and began to produce crystal *t*- $ZrO_2$  since two wide and low peaks were detected at *ca.* 30° and 50°, respectively.

### 2.2 Preparation of $ZrB_2$ –SiBCN– $ZrO_2$ ceramics

Commercial  $ZrB_2$  powder with a particle size range of 0.5–1 µm was produced by ENO High-tech Material Development Co., Qinhuangdao, China (a purity of 99%). Liquid polyborosilazane (PBSZ) as the precursor of SiBCN ceramic, was obtained from the Institute of Chemistry, Chinese Academy of Sciences. After heat treatment at 1000 °C, PBSZ finished primary pyrolysis and generated amorphous SiBCN. With increasing temperature, the amorphous phase underwent structural evolution, resulting in the formation of nanocrystal SiC,  $Si_3N_4$ , C, and BN. The detailed property of the polymer and polymer derived SiBCN was reported in Refs. [10,31]. The weight ratio of  $ZrB_2$  powder and the precursor was fixed to be 92.2:7.8 in order to obtain a composition of 80 vol%  $ZrB_2$  and 20 vol% SiBCN, based on the polymer yield of 76.9% pyrolyzed at 1000 °C.  $ZrO_2$  powder with three different content, namely, 1 wt%, 3 wt%, and 5 wt% was introduced into

the ZrB<sub>2</sub>–SiBCN system. The corresponding samples were denoted as 1-ZrB<sub>2</sub>–SiBCN–ZrO<sub>2</sub>, 3-ZrB<sub>2</sub>–SiBCN–ZrO<sub>2</sub>, and 5-ZrB<sub>2</sub>–SiBCN–ZrO<sub>2</sub>. ZrB<sub>2</sub>–SiBCN sample without ZrO<sub>2</sub> was also prepared for comparison.

ZrB<sub>2</sub> powder, liquid PBSZ, and ZrO<sub>2</sub> powder with n-hexane were mixed by ball milling at 240 rpm for 1.5 h. Then the mixture was dried by removing the n-hexane in vacuum atmosphere. The dried powder was put in a graphite mold and pre-pressed into a green body with a pressure of 40 MPa for 5 min. Then the mold with the sample was moved into a hot-pressing furnace. From room temperature to 1000 °C, the heating rate was set as 10 °C/min and from 1000 to 1600 °C, it was set as 5 °C/min. The load of 2200 kg (ca. 40 MPa) was applied on the sample by means of a hydraulic actuator. The pressure began at 800 °C when the pyrolysis of the polymer was almost accomplished. After holding at 1600 °C for 15 min, the heat and pressure stopped. In order to study the densification progress at different temperature stages, the sample 1-ZrB<sub>2</sub>–SiBCN–ZrO<sub>2</sub> was chosen and sintered at three target temperatures including 1300, 1400, and 1600 °C for 90 min. The whole sintering process was carried out in Ar atmosphere. The displacement change of the samples in the loading direction was recorded. The precision of the displacement is 0.02 mm.

### 2.3 Characterization

The volume density and open porosity of the prepared samples were measured by the Archimedes method. The theoretical density of the composites was estimated by the rule of mixtures based on the theoretical density of zirconium-containing phases (6.10 g/cm<sup>3</sup> for ZrB<sub>2</sub>, 5.82 g/cm<sup>3</sup> for ZrO<sub>2</sub>) and varying densities of polymer-derived SiBCN at different temperatures (2.39 g/cm<sup>3</sup> at 1300 °C, 2.42 g/cm<sup>3</sup> at 1400 °C, 2.62 g/cm<sup>3</sup> at 1600 °C). The dynamic relative density with increasing temperature and time during the densification

process was estimated by the following Eq. (5):

$$D = \frac{D_f}{D_t} \frac{H_f}{H} \times 100\% \tag{5}$$

where *D* is the instantaneous relative density at any temperature or time during hot-pressing process, *D<sub>f</sub>* is the final volume density of the obtained samples, *D<sub>t</sub>* is the theoretical density, *H<sub>f</sub>* is the final height of the samples, and *H* is the instantaneous height. The detailed explanation about relative density was reported in Ref. [10]. The oxygen content of the raw ZrB<sub>2</sub> powder was measured by hot gas extraction technique through a LECO TC-436 analyzer (LECO Corporation St. Joseph, Michigan, America). The phase compositions of the samples were identified by X-ray diffraction (XRD, D/max-2500, Rigaku, Tokyo, Japan) with Cu Kα radiation. The microstructure and morphology were observed by scanning electron microscopy (SEM, JSM7500, Jeol, Tokyo, Japan) equipped with an energy dispersive spectroscopy (EDS).

## 3 Results

### 3.1 Density and open porosity of ZrB<sub>2</sub>–SiBCN based samples

Main hot-pressing parameters, densities, and open porosities of the obtained samples are listed in Table 1. With increasing temperature from 1300 to 1600 °C, the relative density of sample 1-ZrB<sub>2</sub>–SiBCN–ZrO<sub>2</sub> increases by about 28%. For this sample sintered at 1600 °C, the density also has an increase when the soak time is prolonged from 15 to 90 min. Compared to ZrB<sub>2</sub>–SiBCN ceramic without ZrO<sub>2</sub>, samples with ZrO<sub>2</sub> have a higher density and lower open porosity. Meanwhile, with the content of ZrO<sub>2</sub> increasing, the relative density has a slight gradual rise whereas the open porosity does not exhibit a big difference.

**Table 1 Main hot-pressing parameters and physical properties of the obtained samples**

Sample	HP parameter			Content of ZrO <sub>2</sub> (wt%)	Bulk density (g/cm <sup>3</sup> )	Theoretical density (g/cm <sup>3</sup> )	Relative density (%)	Open porosity (%)
	(°C)	(min)	(MPa)					
1-ZrB <sub>2</sub> –SiBCN–ZrO <sub>2</sub>	1300	90	40	1	3.78±0.02	5.36	70.5	30.17±0.20
	1400	90	40	1	4.18±0.05	5.37	77.8	19.34±1.21
	1600	90	40	1	5.35±0.02	5.41	98.9	0.84±0.66
	1600	15	40	1	5.21±0.03	5.41	96.3	1.78±0.75
3-ZrB <sub>2</sub> –SiBCN–ZrO <sub>2</sub>	1600	15	40	3	5.27±0.04	5.42	97.2	1.94±0.42
5-ZrB <sub>2</sub> –SiBCN–ZrO <sub>2</sub>	1600	15	40	5	5.32±0.05	5.42	98.2	2.17±0.78
ZrB <sub>2</sub> –SiBCN	1600	15	40	0	5.12±0.06	5.40	94.8	4.37±1.13

### 3.2 Phase identification and microstructure of $ZrB_2$ -SiBCN- $ZrO_2$ samples

Figure 1 presents the XRD patterns of the obtained  $ZrB_2$ -SiBCN ceramics with different content of  $ZrO_2$  sintered at 1600 °C for 15 min. The main phase in the composites is  $ZrB_2$ . The typical peaks of  $m$ - $ZrO_2$  are detected in all  $ZrO_2$  introduced samples. It has been mentioned above that the obtained  $ZrO_2$  powder as initial additive is almost amorphous and tends to form  $t$ - $ZrO_2$  crystal. With the temperature increasing, the  $t$ - $ZrO_2$  phase gradually transforms into  $m$ - $ZrO_2$  [32]. The process of phase transformation almost finishes at *ca.* 1000 °C [33]. Therefore  $m$ - $ZrO_2$  is involved in the present composites. Additionally, SiC exists in all samples although the intensity of its pattern is quite weak compared with that of  $ZrB_2$ . It is noted that  $ZrB_2$ -SiBCN sample in this work possesses a different phase composition from sample in the previous work [10] which involved  $ZrB_2$ ,  $ZrC$ ,  $ZrO_2$ , SiC, and C. Three reasons are summarized. Firstly, the volume percentage of polymer-derived SiBCN is decreased from 30% to 20%. SiC is generally attributed to the gradual crystallization of amorphous SiBCN network. Thus the low content of SiBCN leads to the low production of SiC. Secondly,  $ZrB_2$  raw powder is changed and the oxygen content of  $ZrB_2$  powder decreases from 4.4 to 1.2 wt%. The purpose is to reduce the effects of oxides from raw materials. The

trace of  $ZrO_2$  crystal in  $ZrB_2$ -SiBCN sample does not appear here. Moreover, the holding time at the sintering temperature (1600 °C) reduces from 2 h to 15 min. Two hours are long enough for SiBCN to separate more SiC crystals as well as for the formation of  $ZrC$  by the reaction between  $ZrO_2$  and C, which would not easily happen in the present situation. As a result, here  $ZrB_2$ -SiBCN based composites have a relatively simple phase composition.

The typical morphology of the  $ZrB_2$ -SiBCN- $ZrO_2$  materials sintered at 1600 °C for 15 min is presented in Fig. 2. From the back-scattered electron (BSE) image in Fig. 2(a), two main phases, bright  $ZrB_2$  grains

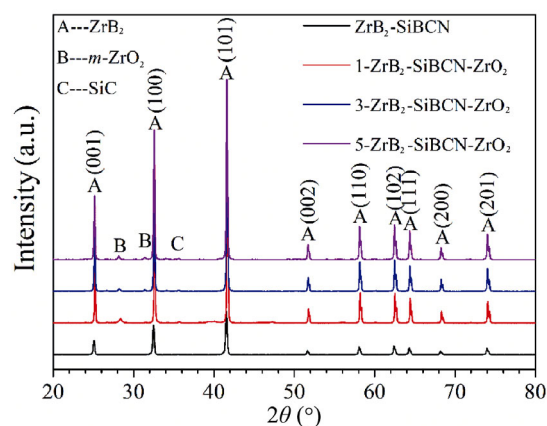


**Fig. 1** XRD patterns of the obtained  $ZrB_2$ -SiBCN ceramics with different content of  $ZrO_2$  sintered at 1600 °C for 15 min.

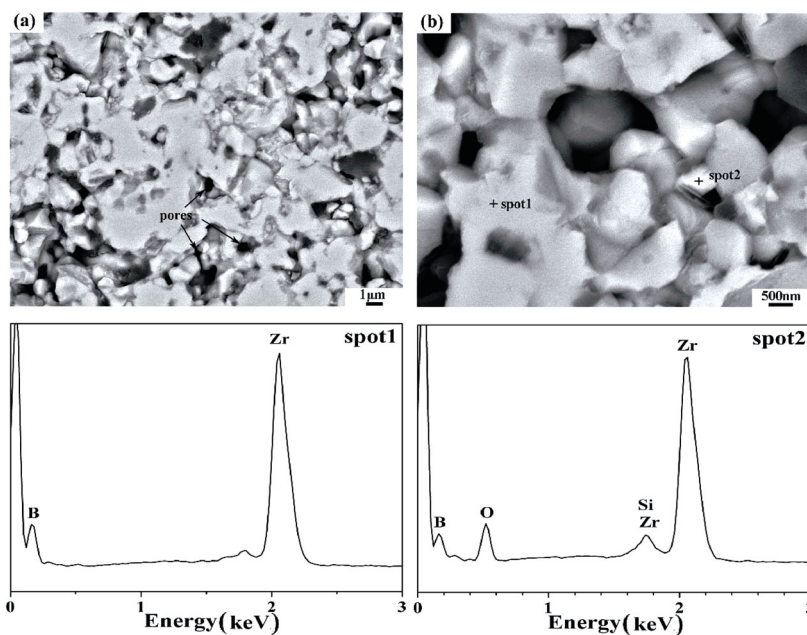


**Fig. 2** Back-scattered electron (BSE) images acquired on the polished section of  $ZrB_2$ -SiBCN ceramics with 5 wt%  $ZrO_2$  sintered at 1600 °C for 15 min and EDS patterns of two spots.

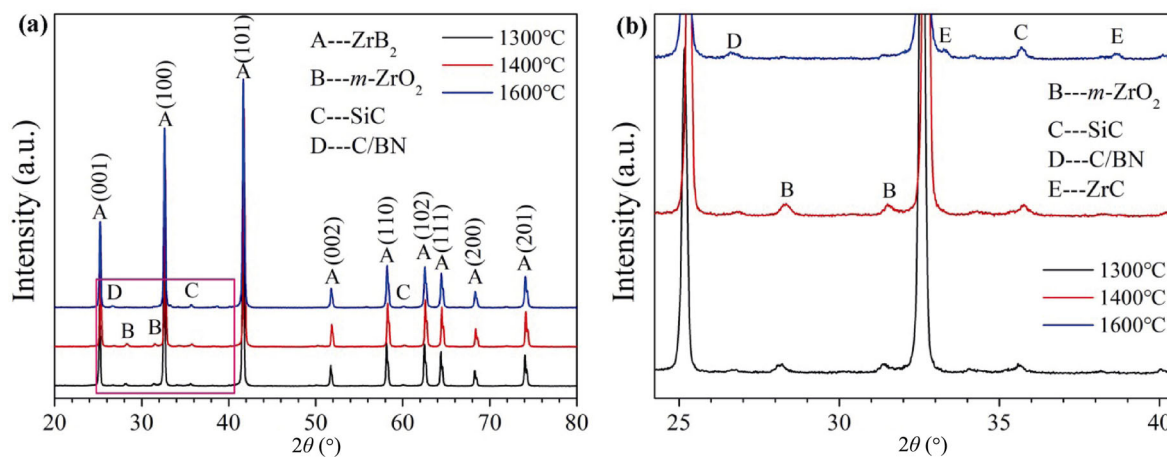
and grey SiBCN products are involved. The grey second phase disperses in the matrix ZrB<sub>2</sub> phase. As shown in Fig. 2(b), ZrO<sub>2</sub> is observed in sample 5-ZrB<sub>2</sub>-SiBCN-ZrO<sub>2</sub>. In the BSE mode, although the composition contrast caused by ZrB<sub>2</sub> and ZrO<sub>2</sub> is not significantly different, some small white particles are recognized as ZrO<sub>2</sub>. The EDS spectra help to confirm that oxygen possesses the atomic percent of 35.42% for spot 2 while only 3.36% oxygen is detected for ZrB<sub>2</sub> particle (spot 1). However, the present sample 5-ZrB<sub>2</sub>-SiBCN-ZrO<sub>2</sub> is not very dense. The microstructure contains apparent defects including cracks and pores located in the second phase or at the interface between two phases.

Something different in phase and microstructure evolution takes place when hot-pressing procedure is refined. Sample 1-ZrB<sub>2</sub>-SiBCN-ZrO<sub>2</sub> is chosen as the target material and sintered at several temperatures (1300, 1400, and 1600 °C) with long heat preservation (90 min). The phase composition with the enlarged patterns between 25° and 40° is displayed in Fig. 3. After sintering at 1300 °C for 90 min, the representative peaks of ZrO<sub>2</sub>, SiC, and C/BN emerge, although they seem weaker compared with those of ZrB<sub>2</sub>. Carbon or *h*-BN generated from the gradual crystallization of SiBCN is involved in the present sample based on the small peak located at 26.6°, which also occurred in previous ZrB<sub>2</sub>-SiBCN samples [10]. When the temperature is increased to 1400 °C, the phases seem little transformation. However, the sample accomplishes a distinct phase change when densified at 1600 °C for 90 min. The peaks of ZrO<sub>2</sub> vanish and those of ZrC are detected, which demonstrates the

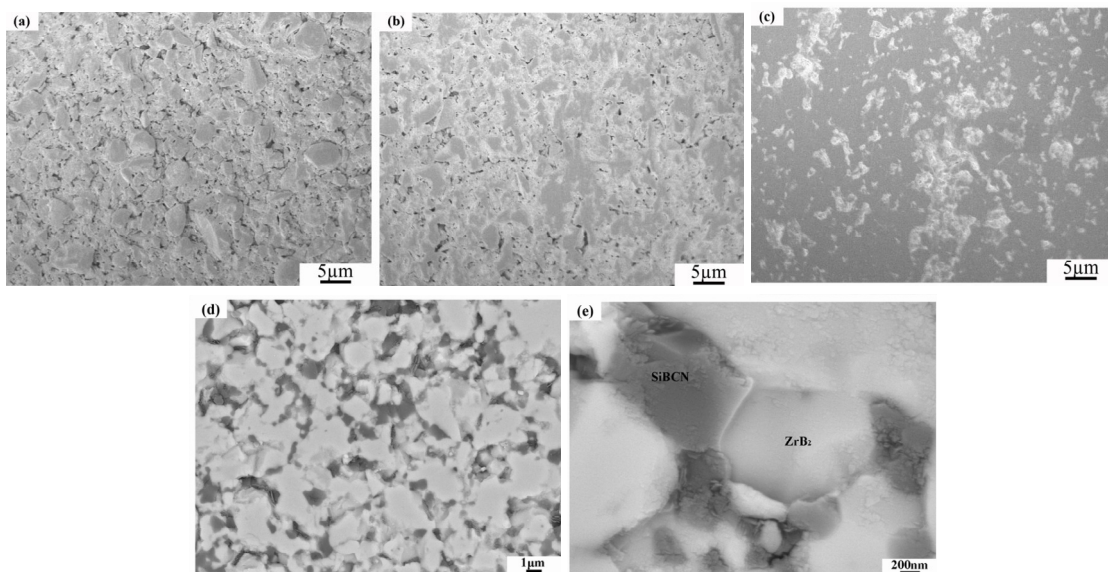
occurrence of carbothermal reduction reaction of ZrO<sub>2</sub> and C. Combined with XRD pattern of the same sample sintered at 1600 °C for 15 min, it indicates that long heat preservation promotes the transformation of ZrO<sub>2</sub> into ZrC, which is a beneficial way to motivate the densification of ZrB<sub>2</sub>-based materials.

Figure 4 shows the microstructure of sample 1-ZrB<sub>2</sub>-SiBCN-ZrO<sub>2</sub> sintered at different temperatures. After hot pressing at 1300 °C for 90 min, the calculated relative density of the sample is 70.5% and the open porosity is *ca.* 30%. It can be seen in Fig. 4(a) there are many visible pores on the polishing surface of the sample. The particles exhibit accumulation state and the pores distribute dispersedly. With higher temperature at 1400 °C, the bulk ceramic becomes evidently denser. The particles fuse together and pore connection occurs, shown in Fig. 4(b). When the temperature is increased continuously, pores are quickly eliminated and the volume of the sample largely shrinks (Fig. 4(c)). The porosity reduces to below 1% after holding for 90 min at 1600 °C. The evolutions of particle aggregation, pore size, and pore distribution reflect the densification progress of the sample.

Further observation in the BSE mode is conducted on the polishing surface of sample 1-ZrB<sub>2</sub>-SiBCN-ZrO<sub>2</sub> sintered at 1600 °C for 90 min. Figures 4(d) and 4(e) show a relatively dense microstructure with clear ZrB<sub>2</sub> and additive SiBCN phases. The interfacial bond between two phases seems well. After longer heat preservation, sample 1-ZrB<sub>2</sub>-SiBCN-ZrO<sub>2</sub> exhibits decreased defects and improved microstructure, compared with BSE images in Fig. 2.



**Fig. 3** (a) XRD patterns of ZrB<sub>2</sub>-SiBCN ceramics with 1 wt% ZrO<sub>2</sub> sintered at different temperatures for 90 min and (b) the large magnification of rectangular area in (a).



**Fig. 4** Microstructure change of ZrB<sub>2</sub>-SiBCN ceramics with 1 wt% ZrO<sub>2</sub> sintered at different temperatures for 90 min: (a) 1300 °C, (b) 1400 °C, (c) 1600 °C, and (d, e) 1600 °C (BSE images with large magnification).

**3.3 Densification behavior of ZrB<sub>2</sub>-SiBCN-ZrO<sub>2</sub> samples**

The relative density changes of typical ZrB<sub>2</sub>-SiBCN-ZrO<sub>2</sub> ceramics with increasing temperature are shown in Fig. 5(a). The global trend of densification among the samples is similar. The initial relative densities after just loading the pressure to the target value are not perfectly the same since they are calculated according to the final respective density. From the densification rate curve (Fig. 5(b)), the density experiences a short rapid increase in early hot-pressing period (900–1050 °C) which corresponds with a compaction stage of green body. Then the densification rate suffers a stable period and the densification curve rises steadily. After 1300 °C fast densification appears,

shown by the rising value of densification rate. This tendency continues until 1600 °C. Especially, ZrB<sub>2</sub>-SiBCN sample with 5 wt% ZrO<sub>2</sub> exhibits faster consolidation above 1400 °C compared to samples with lower content of ZrO<sub>2</sub>. In the present study, oxide is intentionally added into the ZrB<sub>2</sub>-SiBCN system. As a result, the relative density has some enhancement and the sintering behaviors present some variations. On one hand, the additive ZrO<sub>2</sub> participates in chemical reactions with the pyrolysis products, shown in Fig. 3, which may make a difference in the structural evolution of polymer-derived SiBCN. On the other hand, ZrO<sub>2</sub> as the second sintering aid may be capable to promote the matter transportation of the main phase ZrB<sub>2</sub>.

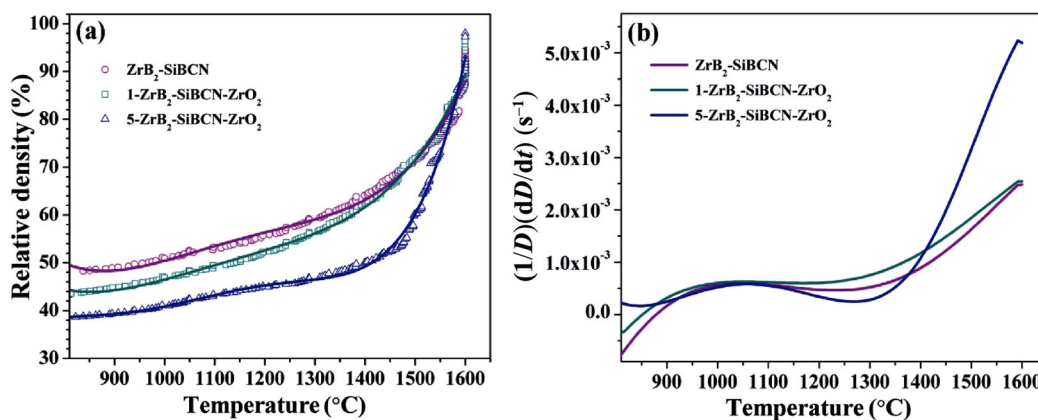


**Fig. 5** (a) Continuous densification and (b) densification rate curves of ZrB<sub>2</sub>-SiBCN ceramics with different contents of ZrO<sub>2</sub> sintered at 1600 °C for 15 min.

The densification kinetics of present material systems is investigated with assist of Bernard-Granger and Guizard model, in order to discuss the possible role of creep deformation in sintering mechanism. Sample 1-ZrB<sub>2</sub>-SiBCN-ZrO<sub>2</sub> is selected as the representative sample and different soak temperatures including 1300, 1400, and 1600 °C are chosen as research interest.

Figure 6(a) shows densification curves of sample 1-ZrB<sub>2</sub>-SiBCN-ZrO<sub>2</sub> during three selected soak temperatures. In accord with the common and intuitive patterns obtained by general ceramic sintering [20,24], the relative density is higher at higher temperatures. Likewise, holding at certain temperature is effective for the further promotion of the densification. Here through holding at 1300, 1400, and 1600 °C for about 90 min the relative density increases by about 7%, 9%, and 11%, respectively. The superiority of temperature is also reflected in densification rate, displayed in Fig. 6(b). The densification rate is relatively larger at 1600 °C at the initial soak stage. However, it cannot maintain a favorable status with the holding time prolonging. The values of the densification rate at all three temperatures decrease and gradually approach zero since driving force of shrinkage for the material is not enough with the growing density and reducing porosity. It is obvious that the densification becomes difficult at the last stage of soak temperature. The holding time of less than 60 min may be preferable for the present system.

## 4 Discussion

### 4.1 Possible densification mechanisms in a view of creep

A key purpose of using Bernard-Granger and Guizard

model is to determine the values of two creep parameters, namely, the stress exponent  $n$  and the apparent activation energy  $Q_d$  in Eq. (4). It is stated that grain size is also temporarily assumed as a constant in this work, since grain growth is closely related to the relative density and the grain size will not visibly vary until a top relative density, for example, close to 98% for a stabilized zirconia ceramic [22]. Additionally, the Young’s modulus ( $E_{th}$ ) of the theoretically dense ZrB<sub>2</sub> material is defined as 490 GPa, and the effective Poisson’s ratio ( $\nu_{eff}$ ) is defined as 0.16 [1,2,34,35]. At this moment the evolution of relative density in function of the holding time for different soak temperatures has been presented in Fig. 6, and then it is possible to have access to the continuous variations of  $\frac{1}{\mu_{eff}} \frac{1}{D} \frac{dD}{dt}$  as a function of  $\frac{\sigma_{eff}}{\mu_{eff}}$ .

Figure 7 depicts this relationship in a logarithmic form. The slopes of different straight lines correspond to  $n$  values.

In Fig. 7 it is clear that  $n$  exhibits different values whatever the soak temperature is. As for 1300 and 1400 °C, there are two distinct linear stages. When  $\ln \frac{\sigma_{eff}}{\mu_{eff}}$  decreases,  $n$  increases in a small range from 1.29 to 2.28 at 1300 °C and from 1.40 to 2.31 at 1400 °C. Then it quickly reaches quite high values which are beyond the effective values. For a soak temperature of 1600 °C, no well-definite linear stages are observed. By linear fitting with some adjacent data,  $n$  is evaluated as 1.78 (close to 2) at the beginning period, bigger than the initial values at lower temperatures. It varies rapidly to 4.95 and subsequent higher values in the following periods. It should be mentioned that at low temperatures  $n$  values are obtained by two linear

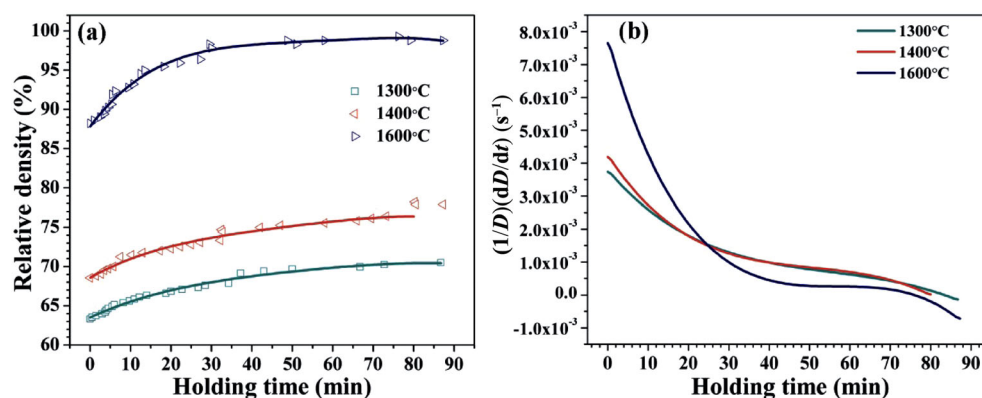
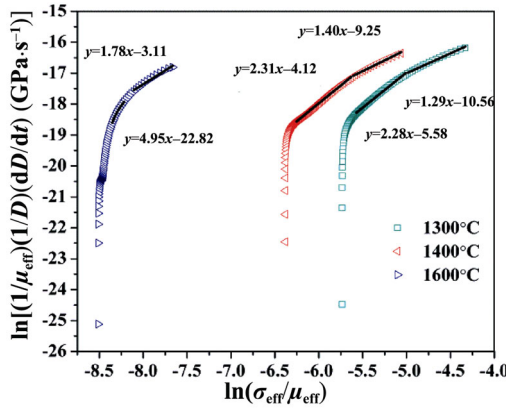
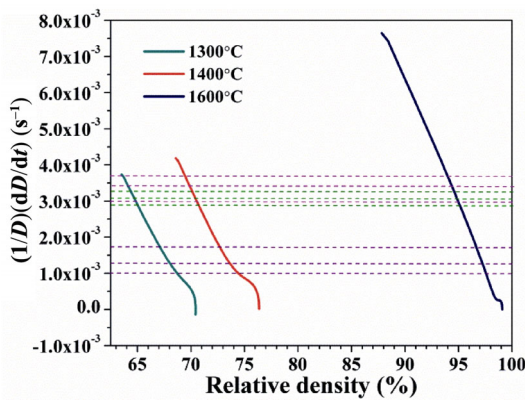


Fig. 6 (a) Densification and (b) densification rate curves of 1-ZrB<sub>2</sub>-SiBCN-ZrO<sub>2</sub> samples obtained at different temperatures with a holding time of 90 min.



**Fig. 7** Stress exponent  $n$  calculated with Eq. (4) for different soak temperatures and the specific values of  $n$  are the slopes of the fitting straight lines.



**Fig. 8** Densification rate as a function of relative density. Three groups of densification rate values are chosen, denoted by pink, purple, and green dotted lines, with purpose of calculating the apparent activation energy ( $Q_d$ ) at different temperatures. The corresponding  $\sigma_{eff}$  and  $\mu_{eff}$  can be obtained according to relative densities upon the fixed values of  $\frac{1}{D} \frac{dD}{dt}$ .

regimes, which means a transition involves. This phenomenon also occurred in the known papers [20,28,29]. However, continuous varying  $n$  values at high temperature are rarely reported. Two possible reasons are summarized. Firstly, varying  $n$  values signify varying densification mechanisms as the mechanism for control of densification in a view of creep deformation is strongly linked to  $n$  value. It seems that sintering at 1300 and 1400 °C for the selected  $ZrB_2$ -SiBCN- $ZrO_2$  system possesses similar densification mechanisms whereas other operating mechanisms may appear for sintering at 1600 °C. Additionally, holding time at certain temperature is relatively long in this material system. The time-dependent effect of creep is fully shown. For previous materials sintered by SPS or HP [20,22], the general holding time was 15 or 20 min and

the calculated values by Bernard-Granger and Guizard model only had one or two linear stages. The relationship between  $n$  and time was not focused on. In the present case, the whole soak period involves as long time as 90 min. Combined results of Fig. 6 and Fig. 7, the soak time of 1300 and 1400 °C can be divided into three stages: 0–15 min (corresponding to  $n \approx 1$ ), 20–55 min (corresponding to  $n \approx 2$ ), and 60–85 min (corresponding to sharply increased  $n$  values). Each stage reveals the status of the densification rate: rapid decrease, steady decrease, and approach to zero. The last status does not coincide with the creep fracture stage which possesses a growing strain rate in a standard creep curve [36]. In the densification process, it just indicates densification comes to a standstill temporarily. In a similar manner, 0–12 min (corresponding to  $n \approx 2$ ), 15–25 min (corresponding to  $n \approx 5$ ), and 30–85 min (corresponding to sharp increased  $n$  values) are assigned for the soak time of 1600 °C. The densification rate experiences a rapid decrease at both of the former two stages and tends to steady status.

The next step is to calculate the apparent activation energy  $Q_d$ . With the value of  $n$  known, we can transform Eq. (4) with a logarithmic method to evaluate  $Q_d$ , shown in Eq. (6):

$$\ln \left[ \frac{T}{\mu_{eff}} \left( \frac{\mu_{eff}}{\sigma_{eff}} \right)^n \frac{1}{D} \frac{dD}{dt} \right] = \frac{-Q_d}{RT} + K_2 \quad (6)$$

where  $K_2$  is a constant. The slope of the straight line obtained by the function relationship between

$$\ln \left[ \frac{T}{\mu_{eff}} \left( \frac{\mu_{eff}}{\sigma_{eff}} \right)^n \frac{1}{D} \frac{dD}{dt} \right] \text{ and } \frac{1}{T} \text{ is equal to } \frac{-Q_d}{R}.$$

Meanwhile,  $\frac{1}{D} \frac{dD}{dt}$  should be determined and then corresponding  $\sigma_{eff}$  and  $\mu_{eff}$  will be known. Thus the relationship between  $\frac{1}{D} \frac{dD}{dt}$  and  $D$  is plotted in Fig. 8.

Based on the two linear stages for the soak temperatures of 1300 and 1400 °C, the value of densification rate can be selected in respective regime, corresponding to respective  $n$  in Fig. 7. Upon approximation, the value of  $n$  within the first linear stage is assumed to be 1 and that within the second linear stage is assumed to be 2. As an example, the chosen densification rate for  $n = 1$  is  $3 \times 10^{-3} \text{ s}^{-1}$  and the one for  $n = 2$  is  $1 \times 10^{-3} \text{ s}^{-1}$ , which is denoted by pink and purple dotted lines in Fig. 8, respectively. Then the corresponding densities at

different temperatures are found, which makes respective  $\sigma_{\text{eff}}$  and  $\mu_{\text{eff}}$  available to be calculated. Finally, the variation of  $\ln \left[ \frac{T}{\mu_{\text{eff}}} \left( \frac{\mu_{\text{eff}}}{\sigma_{\text{eff}}} \right)^n \frac{1}{D} \frac{dD}{dt} \right]$  as a function of  $\frac{1}{T}$  is obtained and shown in Fig. 9.

Two problems are encountered during the selection of densification rate. Firstly, the stage of  $n = 1$  does not exist or is too short to highlight for the soak temperature of 1600 °C. Within this stage ( $n = 1$ ), the fixed densification rate is only effective for 1300 and 1400 °C. Then we choose three fixed densification rates (pink dotted lines in Fig. 8) and obtain three scatters at each temperature. After linking the corresponding scatters, three straight lines are observed to be nearly parallel, shown in Fig. 9. Thus  $Q_d$  is calculated as  $123 \pm 5$  kJ/mol when  $n = 1$ .

The other problem appears for the next stage,  $n = 2$ . Although this stage exists at all the three temperatures, interestingly, it is impossible to find the same densification rates within their respective stage of  $n=2$ . It is supposed that  $Q_d$  may also change in the temperature range of 1300 and 1600 °C since the evidence about the rapid variation of  $n$  values is captured at 1600 °C, based on the above discussion about Fig. 7. As a result, data have been dealt with separately. Actually it is easy to find the same densification rates (purple dotted lines in Fig. 8) within the stage of  $n = 2$  at temperatures of 1300 and 1400 °C. In a similar way as  $n = 1$ , three straight lines are plotted and  $Q_d$  between 1300 and 1400 °C is  $249 \pm 5$  kJ/mol. However, within this stage at 1400 and 1600 °C, the equal densification rates cannot be easily found. Finally,

the series of the same data (green dotted lines in Fig. 8) are chosen in the transition stage between  $n = 1$  and  $n = 2$  for 1400 °C as well as the transition stage between  $n = 2$  and slightly higher  $n$  values for 1600 °C. Then an approximate  $Q_d$  at temperatures above 1400 °C is calculated to be  $597 \pm 9$  kJ/mol.

For the first stage with relatively high effective compaction stresses and low temperature range,  $n$  is around 1 and  $Q_d$  is  $123 \pm 5$  kJ/mol. For the second stage with low effective compaction stresses,  $n$  is around 2 and  $Q_d$  is  $249 \pm 5$  kJ/mol at 1300–1400 °C and  $597 \pm 9$  kJ/mol at higher temperatures. The activation energies seem to be comparable with the values of 63–127 kJ/mol at temperatures below 1350 °C and 450–490 kJ/mol at higher temperature range from 1350 to 1450 °C for ZrB<sub>2</sub>-SiC-(Si<sub>3</sub>N<sub>4</sub>) composites under compressive creep load of 109–141 MPa [37]. The study of post-creep microstructure and analysis of apparent activation energy showed that creep deformation was attributed to grain boundary sliding which was accommodated by O<sup>2-</sup> diffusion across the amorphous SiO<sub>2</sub>-rich film below 1350 °C and by viscoplastic flow of the film above 1350 °C. The creep behavior was largely dependent on the amorphous oxide scale which was generated from the oxidation of the sample surface during deformation process in air. Compared with the study, mechanisms controlling densification in our case have some similarities due to the similar features in compositions, microstructure as well as evaluation method.

In this work, a large amount of polymer precursor with 20 vol% SiBCN is intentionally introduced into ZrB<sub>2</sub> powder. In the temperature range of 1300–1400 °C, polymer-derived SiBCN basically keeps amorphous morphology with an open network structure [10,31]. The atom movement is greatly active and the structure tends to rearrangement. At the beginning of the soak duration, the bulk densities of the composited ceramic are low, which results in relatively high effective compaction stresses based on Eq. (2). However, it was reported that pure ZrB<sub>2</sub> ceramic under compression creep in argon atmosphere showed negligible deformation at 1400 °C [38]. Thus primary deformation of the composite ZrB<sub>2</sub>-SiBCN ceramic happens to the amorphous SiBCN. It is inferred that the operative densification mechanism at this stage ( $n = 1$ ) is grain boundary sliding caused by the atom diffusion of the amorphous SiBCN.

With the holding time prolonged or the temperature

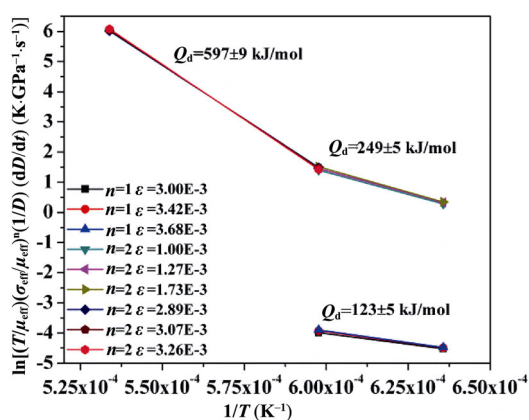


Fig. 9 Apparent activation energy ( $Q_d$ ) as a function of temperature, calculated within different  $n$  values. The slope of the straight lines is  $-Q_d/R$ .

increasing, the viscosity of the amorphous SiBCN varies gradually. It has been known that PDCs possess higher creep resistance than pure vitreous silica. The glass transition temperature of polymer-derived amorphous Si(B)CN is commonly high (e.g., > 1700 °C for Si<sub>2</sub>B<sub>1</sub>C<sub>3,4</sub>N<sub>2,3</sub>, 1400–1500 °C for Si<sub>1.7</sub>C<sub>1.0±0.1</sub>N<sub>1.5</sub>) [13,14] whereas it reduces significantly when oxygen is involved, for instance, 1350–1400 °C for SiOC ceramic [17]. The present material system involves 1 wt% ZrO<sub>2</sub>. The lattice/volume diffusion of Zr<sup>4+</sup> and O<sup>2-</sup> always attracted much attention in zirconium polycrystals. Especially the grain boundary diffusion of cations (Zr<sup>4+</sup> or Y<sup>3+</sup>) was considered to control the high-temperature deformation of yttria-stabilized zirconia powder during SPS or HP sintering [20,22]. Thus it is proposed that the active O<sup>2-</sup> enters into the open amorphous structure of SiBCN and substitutes some locations of C, which leads to the decrease of viscosity of the second phase. The chemical bond of Si–O was clearly detected by FT-IR in the previous study on ZrB<sub>2</sub>–SiBCN composites [10]. At this stage ( $n = 2$ ), grain boundary sliding accommodated by viscous flow of the amorphous second phase becomes more dominant compared to the former stage.

With the temperature increasing continuously, the apparent activation energy increases and approaches to 600 kJ/mol. Based on the above discussion, the viscous flow effectiveness of polymer-derived SiBCN should have enhanced. If the amorphous SiBCN possesses excellent high-temperature stability and resistance to crystallization until 1600 °C, the viscosity of it would decrease to 10<sup>14</sup> Pa·s [13]. Doping oxygen may promote the further decrease of viscosity and make viscoplastic flow more favorable. However, the present SiBCN is not capable to keep predominantly amorphous and it always experiences phase separation and crystallization upon the elevated temperatures. Actually weak crystal peaks of SiC have been traced after long time duration of 1300 °C according to the XRD results in Fig. 3. Based on the general crystallization behavior of amorphous ceramic doped with contamination particles [39], the doped impurity (ZrO<sub>2</sub>) may be beneficial to decrease the nucleation rate of amorphous SiBCN by means of increasing part of driving force necessary for the diffusion and rearrangement process of atoms, but it can also enhance the growth rate of the formed crystals. Moreover, the diffusion of O<sup>2-</sup> leads to the occurrence of carbothermal reduction reaction between ZrO<sub>2</sub> and C atom at the soak temperature of

1600 °C, which accelerates the decomposition reaction of SiBCN. As a result, crystal SiC and ZrC are produced at the expense of the gradual consumption of amorphous SiBCN. It was reported that the deformation rate for the annealed SiBCN was much lower than the amorphous ceramic under compression tests [11,15]. Therefore, the operative deformation mechanism transforms from grain boundary fluidity to lattice or intra-granular diffusion creep with little glassy or amorphous phase. The creep deformation is always related to the motion of dislocations like glide and climb [24,29,37], which corresponds to values of  $n$  in the range of 3–5. It is stressed that the proposed mechanisms controlling densification are not absolutely independent as the densification process itself includes overlapped stages such as formation of grain boundary and interface, pore rounding, and pore closure. The variation of amorphous SiBCN in amount and viscosity as well as the formation of crystals results in the transition in mechanisms, which is responded by the continuously varying  $n$  values in Fig. 7.

#### 4.2 Effects of ZrO<sub>2</sub> content on the densification

We have found that ZrO<sub>2</sub> as a main oxide existing in ZrB<sub>2</sub>–SiBCN system can react with the pyrolysis carbon generated from the polymer-derived SiBCN, which is beneficial for the densification of the composites [10]. In this work, the carbothermal reduction reaction has also been detected with evidence of the formation of ZrC, which occurs upon the soak duration of 1600 °C, reflected in Fig. 3. Besides, it has been proposed that the diffusion of O<sup>2-</sup> into the amorphous SiBCN contributes to modifying its viscosity before occurrence of the reaction. We still wonder whether the content of the oxides has a limit.

ZrB<sub>2</sub>–SiBCN ceramics with different contents of ZrO<sub>2</sub> are sintered at 1300 °C for 90 min. The densification curves and the corresponding densification rate curves are shown in Fig. 10. All the samples exhibit the known similar behavior which involves accelerated densification at the beginning and moderate densification in the following period. The relative density increases by around 5%, 7%, and 3% for ZrB<sub>2</sub>–SiBCN, 1-ZrB<sub>2</sub>–SiBCN–ZrO<sub>2</sub>, and 5-ZrB<sub>2</sub>–SiBCN–ZrO<sub>2</sub>, respectively. The rising degree is not as obvious as that at elevated temperatures (Fig. 6(a)). The sample with composition of 1-ZrB<sub>2</sub>–SiBCN–ZrO<sub>2</sub> shows preferable sintering potential at this temperature. From Fig. 10(b), the densification rate of 1-ZrB<sub>2</sub>–SiBCN–ZrO<sub>2</sub> is the highest

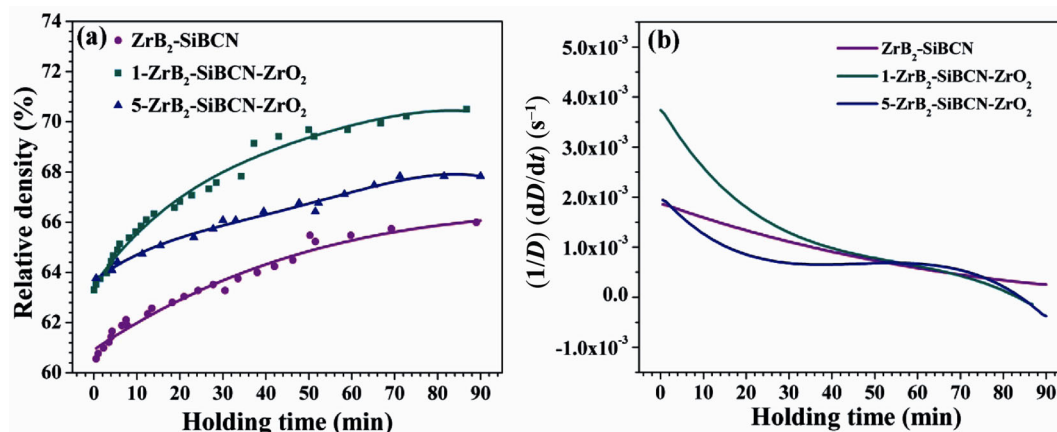


**Fig. 10** (a) Densification and (b) densification rate of ZrB<sub>2</sub>-SiBCN ceramics with different contents of ZrO<sub>2</sub> at soak temperature of 1300 °C for around 90 min.

within the first 50 min whereas that of 5-ZrB<sub>2</sub>-SiBCN-ZrO<sub>2</sub> is the lowest. At the last stage of duration, the densification rates have no obvious differences.

It seems that the introduction of ZrO<sub>2</sub> does not develop significantly helpful effects on the densification at such a low temperature. As we have discussed above, grain boundary sliding accommodated by the atom diffusion and by viscous flow of the amorphous SiBCN phase is mainly responsible for the densification rate at the initial and medium soak regimes, respectively. When 1 wt% ZrO<sub>2</sub> is introduced into ZrB<sub>2</sub>-SiBCN based composites, ZrO<sub>2</sub> attempts to join into the structure of SiBCN by ion diffusion and modifies the viscous flow of amorphous SiBCN. Consequently, sample 1-ZrB<sub>2</sub>-SiBCN-ZrO<sub>2</sub> shows relatively high densification rates. However, when the content of ZrO<sub>2</sub> is increased to 5 wt%, the densification effectiveness is not improved. It indicates that in this period the amount of the ions capable to diffuse into the SiBCN network may be limited. Irrespective of the interaction between oxides and the amorphous phase, ZrO<sub>2</sub> itself is difficult to densify at the low temperature of 1300 °C. The incorporation of more ZrO<sub>2</sub> crystal particles is not beneficial for enhancing the densification proceeding at this moment.

At higher temperatures, promotions in densification induced by more content of ZrO<sub>2</sub> stand out gradually. From Fig. 5, the densification rate of ZrB<sub>2</sub>-SiBCN with 5 wt% ZrO<sub>2</sub> begins to rise sharply from 1350 °C. The tendency maintains until 1600 °C. The results lead to the following inferences. When the temperature increases, the amorphous SiBCN network can receive more ions inside ZrO<sub>2</sub> and the viscosity of the second phase decreases obviously. As a consequence, the

subsequent high densification efficiency of sample 5-ZrB<sub>2</sub>-SiBCN-ZrO<sub>2</sub> is attributed to the grain boundary sliding accommodated by stable viscous flow of the second phase. It implies that the densification proceeding is slightly delayed by the increasing content of ZrO<sub>2</sub>. Additionally, it is observed from the SEM image in Fig. 2 that a few ZrO<sub>2</sub> particles disperse in ZrB<sub>2</sub> and SiBCN phases for sample 5-ZrB<sub>2</sub>-SiBCN-ZrO<sub>2</sub>. The formation of grain boundaries between ZrO<sub>2</sub> and ZrB<sub>2</sub> or SiBCN indicates that the increased grain boundaries also make a contribution to the further consolidation of the material.

## 5 Conclusions

In this work, hot-pressing ZrB<sub>2</sub>-SiBCN-ZrO<sub>2</sub> ceramics under a constant applied pressure of 40 MPa involve a clear creep deformation. The densification behavior of the composites has been evaluated with emphasis on the creep mechanisms based on Bernard-Granger and Guizard model. At lower temperatures of 1300–1400 °C, the operative deformation mechanism is grain boundary sliding, accommodated by atom diffusion of the polymer-derived SiBCN ( $n = 1$ ,  $Q_d = 123 \pm 5$  kJ/mol) and by viscous flow of the amorphous SiBCN doped with ZrO<sub>2</sub> ( $n = 2$ ,  $Q_d = 249 \pm 5$  kJ/mol). With the temperature increasing, amorphous SiBCN phase gradually consumes and  $Q_d$  increases to  $597 \pm 9$  kJ/mol. At a soak temperature of 1600 °C, the controlling mechanism transformed into lattice or intra-granular diffusion creep of the solid particles ( $n = 3-5$ ).

It is supposed that a small amount of ZrO<sub>2</sub> (1 wt%) enters into the polymer-derived SiBCN by ionic diffusion and enhances the viscous flow of the amorphous phase,

which improves the deformation performance of ZrB<sub>2</sub> based materials.

### Acknowledgements

Financial support from the National Natural Science Foundation of China (Grant No. 51272009) is sincerely acknowledged.

### References

- [1] Guo SQ. Densification of ZrB<sub>2</sub>-based composites and their mechanical and physical properties: A review. *J Eur Ceram Soc* 2009, **29**: 995–1011.
- [2] Fahrenholtz WG, Hilmas GE, Talmy IG, *et al.* Refractory diborides of zirconium and hafnium. *J Am Ceram Soc* 2007, **90**: 1347–1364.
- [3] Chamberlain AL, Fahrenholtz WG, Hilmas GE. Pressureless sintering of zirconium diboride. *J Am Ceram Soc* 2006, **89**: 450–456.
- [4] Monteverde F, Bellosi A, Scatteia L. Processing and properties of ultra-high temperature ceramics for space applications. *Mat Sci Eng A* 2008, **485**: 415–421.
- [5] Krishnarao RV, Bhanuprasad VV, Madhusudhan Reddy G. ZrB<sub>2</sub>-SiC based composites for thermal protection by reaction sintering of ZrO<sub>2</sub>+B<sub>4</sub>C+Si. *J Adv Ceram* 2017, **6**: 320–329.
- [6] Monteverde F, Bellosi A, Guicciardi S. Processing and properties of zirconium diboride-based composites. *J Eur Ceram Soc* 2002, **22**: 279–288.
- [7] Ahmadi Z, Nayebi B, Shahedi Asl M, *et al.* Sintering behavior of ZrB<sub>2</sub>-SiC composites doped with Si<sub>3</sub>N<sub>4</sub>: A fractographical approach. *Ceram Int* 2017, **43**: 9699–9708.
- [8] Asl MS, Nayebi B, Ahmadi Z, *et al.* Effects of carbon additives on the properties of ZrB<sub>2</sub>-based composites: A review. *Ceram Int* 2018, **44**: 7334–7348.
- [9] Zhang ZF, Sha JJ, Zu YF, *et al.* Fabrication and mechanical properties of self-toughening ZrB<sub>2</sub>-SiC composites from *in situ* reaction. *J Adv Ceram* 2019, **8**: 527–536.
- [10] Feng B, Zhang Y, Li BY, *et al.* Medium-temperature sintering efficiency of ZrB<sub>2</sub> ceramics using polymer-derived SiBCN as a sintering aid. *J Am Ceram Soc* 2019, **102**: 855–866.
- [11] Colombo P, Mera G, Riedel R, *et al.* Polymer-derived ceramics: 40 years of research and innovation in advanced ceramics. *J Am Ceram Soc* 2010, **93**: 1805–1837.
- [12] Stabler C, Ionescu E, Graczyk-Zajac M, *et al.* Silicon oxycarbide glasses and glass-ceramics: “All-Rounder” materials for advanced structural and functional applications. *J Am Ceram Soc* 2018, **101**: 4817–4856.
- [13] Riedel R, Ruswisch LM, An LN, *et al.* Amorphous silicoboron carbonitride ceramic with very high viscosity at temperatures above 1500°C. *J Am Ceram Soc* 1998, **81**: 3341–3344.
- [14] An LN, Riedel R, Konetschny C, *et al.* Newtonian viscosity of amorphous silicon carbonitride at high temperature. *J Am Ceram Soc* 1998, **81**: 1349–1352.
- [15] Ravi Kumar NV, Mager R, Cai Y, *et al.* High temperature deformation behaviour of crystallized Si–B–C–N ceramics obtained from a boron modified poly(vinyl)silazane polymeric precursor. *Scripta Mater* 2004, **51**: 65–69.
- [16] Ravi Kumar NV, Prinz S, Cai Y, *et al.* Crystallization and creep behavior of Si–B–C–N ceramics. *Acta Mater* 2005, **53**: 4567–4578.
- [17] Stabler C, Roth F, Narisawa M, *et al.* High-temperature creep behavior of a SiOC glass ceramic free of segregated carbon. *J Eur Ceram Soc* 2016, **36**: 3747–3753.
- [18] Zhang PF, Yang B, Lu Z, *et al.* Effect of AlN and ZrO<sub>2</sub> on the microstructure and property of the 2Si–B–3C–N ceramic. *Ceram Int* 2018, **44**: 3406–3411.
- [19] Ionescu E, Linck C, Fasel C, *et al.* Polymer-derived SiOC/ZrO<sub>2</sub> ceramic nanocomposites with excellent high-temperature stability. *J Am Ceram Soc* 2010, **93**: 241–250.
- [20] Bernard-Granger G, Addad A, Fantozzi G, *et al.* Spark plasma sintering of a commercially available granulated zirconia powder: Comparison with hot-pressing. *Acta Mater* 2010, **58**: 3390–3399.
- [21] Zhang JY, Zhan H, Fu ZY, *et al.* *In-situ* synthesis and sintering of mullite glass composites by SPS. *J Adv Ceram* 2014, **3**: 165–170.
- [22] Bernard-Granger G, Guizard C. Spark plasma sintering of a commercially available granulated zirconia powder: I. Sintering path and hypotheses about the mechanism(s) controlling densification. *Acta Mater* 2007, **55**: 3493–3504.
- [23] Coble RL. Diffusion models for hot pressing with surface energy and pressure effects as driving forces. *J Appl Phys* 1970, **41**: 4798–4807.
- [24] Kashyap SK, Mitra R. Densification behavior involving creep during spark plasma sintering of ZrB<sub>2</sub>-SiC based ultra-high temperature ceramic composites. *Ceram Int* 2020, **46**: 5028–5036.
- [25] Mukherjee A, Bird JE, Dorn JE. Experimental correlations for high-temperature creep. Lawrence Berkeley National Laboratory. 1968, LBNL Report #: UCRL-18526.
- [26] Helle AS, Easterling KE, Ashby MF. Hot-isostatic pressing diagrams: New developments. *Acta Metall* 1985, **33**: 2163–2174.
- [27] Lam DCC, Lange FF, Evans AG. Mechanical properties of partially dense alumina produced from powder compacts. *J Am Ceram Soc* 1994, **77**: 2113–2117.
- [28] Chawake N, Koundinya NTBN, Srivastav AK, *et al.* On correlation between densification kinetics during spark plasma sintering and compressive creep of B2 aluminides. *Scripta Mater* 2015, **107**: 63–66.
- [29] Ramond L, Bernard-Granger G, Addad A, *et al.* Sintering of a quasi-crystalline powder using spark plasma sintering and hot-pressing. *Acta Mater* 2010, **58**: 5120–5128.

- [30] Liu GH, Li RD, Yuan TC, *et al.* Spark plasma sintering of pure TiCN: Densification mechanism, grain growth and mechanical properties. *Int J Refract Met Hard Mater* 2017, **66**: 68–75.
- [31] Zhang ZB, Zeng F, Han JJ, *et al.* Synthesis and characterization of a new liquid polymer precursor for Si–B–C–N ceramics. *J Mater Sci* 2011, **46**: 5940–5947.
- [32] Garvie RC. Stabilization of the tetragonal structure in zirconia microcrystals. *J Phys Chem* 1978, **82**: 218–224.
- [33] Li HB, Liang KM, Gu SR. Stability of *t*-ZrO<sub>2</sub> in zirconia powder prepared by sol–gel process. *J Tsinghua Univ (Sci & Tech)* 2001, **41**: 13–15.
- [34] Guo SQ, Kagawa Y, Nishimura T, *et al.* Elastic properties of spark plasma sintered (SPSed) ZrB<sub>2</sub>–ZrC–SiC composites. *Ceram Int* 2008, **34**: 1811–1817.
- [35] Guo SQ, Nishimura T, Mizuguchi T, *et al.* Mechanical properties of hot-pressed ZrB<sub>2</sub>–MoSi<sub>2</sub>–SiC composites. *J Eur Ceram Soc* 2008, **28**: 1891–1898.
- [36] Talmy IG, Zaykoski JA, Martin CA. Flexural creep deformation of ZrB<sub>2</sub>/SiC ceramics in oxidizing atmosphere. *J Am Ceram Soc* 2008, **91**: 1441–1447.
- [37] Mallik M, Ray KK, Mitra R. Effect of Si<sub>3</sub>N<sub>4</sub> addition on compressive creep behavior of hot-pressed ZrB<sub>2</sub>–SiC composites. *J Am Ceram Soc* 2014, **97**: 2957–2964.
- [38] Meléndez-Martínez J, Domínguez-Rodríguez A, Monteverde F, *et al.* Characterisation and high temperature mechanical properties of zirconium boride-based materials. *J Eur Ceram Soc* 2002, **22**: 2543–2549.
- [39] Kingery WD, Bowen HK, Uhlmann DR. *Introduction to Ceramics*, 2nd edn. New York: Wiley, 1976.

**Open Access** This article is licensed under a Creative Commons Attribution 4.0 International License, which permits use, sharing, adaptation, distribution and reproduction in any medium or format, as long as you give appropriate credit to the original author(s) and the source, provide a link to the Creative Commons licence, and indicate if changes were made.

The images or other third party material in this article are included in the article's Creative Commons licence, unless indicated otherwise in a credit line to the material. If material is not included in the article's Creative Commons licence and your intended use is not permitted by statutory regulation or exceeds the permitted use, you will need to obtain permission directly from the copyright holder.

To view a copy of this licence, visit <http://creativecommons.org/licenses/by/4.0/>.